

A Computational Fluid Dynamics Study on Physical Refining of Steel Melts by Filtration

Shahin Akbarnejad, Dong-Yuan Sheng and Pär Göran Jönsson

Department of Materials Science and Engineering, Royal Institute of Technology (KTH), Stockholm, Sweden

* Communicating author: shahinak@kth.se

In this paper, a previous experimental investigation on physical refining of steel melts by filtration was numerically studied. To be specific, filtration of non-metallic alumina inclusions, in the size range of 1 to 100 [μm], from steel melt by using a square-celled monolithic alumina filter was simulated. Computational fluid dynamics (CFD) studies, including simulations of both fluid flow and particle tracing using one-way coupling method, were conducted. The CFD predicted results for particles in the size range ≤ 5 [μm] were compared to the published experimental data. The modelled filtration setup could capture 100 % of the particles larger than 50 [μm]. The percentage of the filtered particles decreases from 98% to 0% in the particle size range of 50 [μm] to 1[μm].

KEY WORDS: Steel refining, Steel filtration, Alumina filters, Ceramic filters

1 Introduction

In metallurgy, ceramic filters are used to remove solid particles and inclusions from molten metals ¹⁻⁴⁾. Inclusions play an important role in the mechanical properties of metallic materials ⁴⁻¹⁰⁾. Sometimes, they are intentionally generated, carefully controlled, and quantified, *i.e.* inclusion engineering, to create a specific type of material with desired mechanical properties ⁹⁾. However, most of the time the main aim is to remove, control, and/or decrease the number of unwanted inclusions ^{4,6,7,10,11)}. Many well-known and established techniques are used to satisfy the demands ^{7,10,12)}. However, there is still an interest to deeper understand the mechanisms of formation and behavior of the inclusions in molten metal and to develop more effective methods which would be practical, simple and cost efficient ^{6,10,11,13)} to remove inclusions from molten metal.

Physical removal of inclusions from molten metal is a well-known phenomenon in production of non-ferrous metals. Particularly, numerous research projects have been conducted and several filtration methods have been developed in aluminum industry ¹⁴⁻¹⁷⁾. However, not many published research works on the physical filtration of molten steel are available. In general, the demand for high quality steel requires removal and control of non-metallic inclusions ^{5,8-11,14,18)}. The volume fraction of non-metallic inclusions depends mainly on the oxygen and sulphur contents of the steel melt ^{5,9,11,19)}. These two elements are generally present as oxides and sulphides in the steel melts and form non-metallic inclusions ^{5,9-11,13)}. To reduce the dissolved oxygen content, deoxidizers such as Al, Fe-Al, Ti, Fe-Si, Fe-Ti, etc. are added to the steel melt ^{11,18,20,21)}. The products of the deoxidization process are various sizes and types of inclusions ^{11,22)}. A fraction of the inclusions are removed during slag refining process. However, the small inclusions could remain in the steel melt and move along in the direction of the bulk flow of the molten steel ^{11,23,24)}. There, collisions between the inclusions occur which result in agglomeration and clustering of alumina inclusions ^{11,20,22,25)}. Among all of the non-metallic inclusions, deposition of alumina inclusions in tundish nozzles is believed to cause reduced molten steel pouring rate and nozzle blockage ^{10,11,20,22,23,26)} while teeming the tundish from steel melts during castings. Therefore, there has been a great interest to find a practical and inexpensive technique to remove or reduce the amount of these inclusions prior to casting and/or while casting.

In 1985, S. Ali et al. ^{10,11,13)} performed several laboratory scale molten steel filtration experiments targeting 5 [μm] alumina inclusions and smaller. In their experiment, two types of filters were used: a) tabular granules of alumina and b) monolithic extruded alumina. It was shown that it is possible to physically remove alumina inclusions with both types of filters. To be specific, it was revealed that lower molten steel flow rates and increased filter heights/ lengths escalates the inclusion removal efficiency.

In 1991, K. Uemura et al. ¹⁴⁾ used ceramic loop filters of different ceramic materials as well as different string diameters to physically remove alumina inclusions and to study the filtration mechanisms. They found that the filter material had no significant effect on filtration efficiency. It was also found that the filtration efficiency depends on the string diameter and initial oxygen content. The highest filtration efficiency could be achieved using a 2 mm diameter string filter media. Here, inclusions in the size range greater than 5 μ m were reduced by filtration.

In 2012, L. Bulkowski et al. ²⁷⁾ performed both laboratory and industrial scale molten steel filtration experiments. They used ceramic corundum and mullite as filter materials. For the laboratory test, it was reported that the surface share of inclusions in filtered steel compared to the un-filtered steel was reduced by 48-50%. The total oxygen content and number of inclusions were reduced by 58% and 38% respectively. In addition, the industrial tests were carried out while downhill casting of molten steel into molds. Here, the maximum surface share of inclusions and number of inclusions were reduced by 33% and 13% respectively. The overall decrease in the oxygen content was also reported to be maximum 75%.

Recently, S. Chakraborty et al. ^{28,29)} used 10 Pore Per Inch (PPI) MgO stabilized zirconia foam filters to study filtration efficiency of solid alumina inclusions from molten steel. The highest overall inclusion efficiency achieved by filtration, while comparing castings produced with and without a filter from the same heat, was reported to be 48%.

The current research aims at developing a reliable CFD model to predict the filtration of inclusions from molten steel. To validate the CFD model, the experimental work on the physical refining of steel melt using monolithic extruded alumina filters by S. Ali et al. ^{10,11,13)} was used.

2 Theoretical Background

2.1 Summary of the physical steel melt refining experiments

S. Ali *et al.* designed an experimental apparatus and a filter setup, and used square-celled monolithic extruded alumina filters to refine steel melts. The schematic view of the experimental apparatus and filter setup, and a picture of the cemented monolithic alumina filter used in the experiments are shown in Figures 1a-1c. Here, a summary of the experimental procedure is explained. Comprehensive explanations of the experimental procedure and apparatus are available elsewhere ^{10,11,13)}.

A steel charge containing 0.012 pct. C, 0.04 Ni and 12 to 20 pct. ppm of oxygen was heated to 1600 \pm 10°C in an argon filled furnace dome. After the charge was melted, the initial desired oxygen content was brought up to 400 to 500 ppm by addition of reagent grade Fe₂O₃ powder to the charge. Then, it was kept for 30 minutes to homogenize the melt. Later, a sample was taken from the center of the melt, and a known amount of high purity aluminum wire was added to the melt. After 3 minutes, a sample

from the center of the melt was taken to obtain the content of the alumina before filtration. Then, the top chamber was pressurized with argon. The alumina stopper rod was removed to let the molten steel flow through the filter setup. The filtered steel then was casted in a metallic mold that was placed in the lower chamber of the apparatus. In their investigation, concentration of alumina inclusions in the unfiltered and filtered steel melts were obtained and compared. Meanwhile, the effects of the square-celled monolithic alumina filter height as well as steel flow rate on the concentration of alumina inclusions in the filtered melts were also studied.

3 Methodology

3.1 Mathematical modelling

To evaluate particle entrapment using Computational Fluid Dynamics (CFD) and to compare the results to the previous experimental findings, a three-dimensional model representing the experimental filtration setup was created. The model simulates a perfectly sealed filter where no gap exists between the filter holder and the filter media. Recently, it was shown that to prevent fluid bypassing the filters need to be properly sealed³⁰⁾. In addition, to avoid simulation and convergence complications, it is also assumed that the filter is made as part of the alumina crucible. Therefore, the alumina spacers shown in Figure 1c were neglected in the CFD model. The model was made according to the actual filter setup and experimental apparatus dimensions as shown in Figure 1 and Table 1 and as explained elsewhere^{10,11,13)}. In addition, the filter matrix, particle and fluid properties, *e.g.* particle density, fluid density, and fluid temperature and dynamic viscosity were set according to the experimental conditions presented in Table 2 and explained elsewhere^{10,11,13,31)}.

To decide upon the fluid flow regime and to choose an appropriate module in the software the Reynolds numbers were calculated. The Reynolds number for the overall flow (R_e) and the particle relative Reynolds number (R_{er}) can be calculated as follows^{32–37)}:

$$R_e = \frac{\rho u l}{\mu} \quad (1)$$

$$R_{er} = \frac{\rho |u - v| d_p}{\mu} \quad (2)$$

where ρ [kg/m³] is the fluid density, u [m/s] is the fluid velocity, l [m] is the characteristic length, μ [Pa·s] is the fluid dynamic viscosity, v [m/s] is the particle velocity, and d_p [m] is the particle diameter. In a pipe like configuration the characteristic length l [m] could be replaced with hydraulic diameter D_h [m].

S. Ali *et al.* measured and reported the interstitial velocity for the various experimental trials. In addition, their experiments included alumina inclusion sizes of 1 to 5 [μ_m]. In this research, the

experimental condition correlating to the interstitial velocity 0.08 [cm/s] for a 5 cm long monolithic alumina filter with a filter porosity ε equal to 0.63 were analytically obtained. Meanwhile, particle trajectories of the alumina inclusions larger than 5 [μm] and up to 100 [μm] were also simulated.

In an incompressible flow where the density is constant, one may use the continuity equation (3). Here, when the interstitial velocity, porosity, inlet, and outlet diameters, as well as number of the pores and pore dimensions are known, one may calculate the flow rates at the inlet, the spacer between the inlet and filter pores, the spacer between the filter pores and outlet and lastly the outlet. The calculated values are: 1.33, 0.07, 0.07 and 214.2 [cm/s] respectively.

$$A_1 V_1 = A_2 V_2 \quad (3)$$

Table 3 presents the calculated particle relative Reynolds numbers. Here, the maximum possible velocity difference was used in calculations to obtain the highest Reynolds number, *i.e.* the velocity difference equals the fluid velocity. The obtained numbers are needed to navigate in selecting adequate forces for calculating particle trajectories. The fluid flow Reynolds numbers at the inlet, filter pore, and outlet were found to be ~226, 1.2, 502 and 2865 respectively. The flow regime at $Re < 2300$ ^{32,34,36)} is considered to be laminar. As a result, in all sections the Reynolds number is less than 2300, except for the outlet. However, the outlet is at the downstream. Therefore, the laminar flow could be applied to the whole domains of the system. As a result, a 2-step simulation to solve the relevant physics was used ³⁵⁾. The first step calculates the steady flow fields through the modelled filter setup. The second step is to calculate the transport of the solid particles using an unsteady solver based on the results obtained from the first step, *i.e.* the steady flow field calculations or unidirectional/one-way coupling ³⁵⁾. For that reason, the “Laminar Flow” and the “Particle Tracing for Fluid Flow” modules in COMSOL Multiphysics® 6.0 software were used. Consequently, the following governing transport equations need to be solved:

- i. The Navier-Stokes equations for incompressible fluids, containing continuity and conservation of momentum,
- ii. The Newton’s second law for the motion of particles in fluid flow.

To compensate for time and calculation memory costs only a quarter of the filter setup was simulated, as shown in Figure 2. An inlet and a spacing section were connected to the top of the filter. Then the lower part of the filter was connected to a spacing section and an outlet. Therefore, the simulated fluid enters the inlet, flows through the spacer and filter pores, and exits the filter, lower spacer, and outlet from the opposite side.

3.2 Assumptions

The following assumptions were made to perform the mathematical modelling:

- i. The fluid, filter and particle properties are identical in all quarters of the whole filter setup
- ii. No fluid bypassing was considered. The filter is made as part of the alumina crucible
- iii. Temperature is assumed to be constant
- iv. The solution is independent of time, i.e. a steady state solution
- v. The gravitational force was considered
- vi. Incompressible Newtonian fluid with constant fluid density and viscosity.
- vii. No heat transfer to/from the ambient medium was considered
- viii. There is no fluid-wall interaction.
- ix. The walls are assumed to be straight and smooth, using a no-slip boundary condition
- x. Fluid-particle interaction was not considered.(unidirectional or one-way coupling)
- xi. Particle-particle interaction was not considered.
- xii. The particles are assumed to be spherical, following the findings of the reference ¹¹⁾.
- xiii. Particles do not displace the fluid they occupy.
- xiv. Properties of the Steel containing 0.012 pct. C, 0.04 Ni was assumed to be the same as Iron at 1873[K].

3.3 The transport equations

In an incompressible, isothermal Newtonian flow, *i.e.* density and viscosity are constant; the steady state fluid flow is described by the Navier-Stokes equations. The Navier-Stokes equations, including the continuity and momentum equations can be written as follows ³⁴⁾:

$$\rho \nabla \cdot (\mathbf{u}) = 0 \quad (4)$$

$$\rho(\mathbf{u} \cdot \nabla) \mathbf{u} = \nabla \cdot [-p\mathbf{I} + \mu(\nabla \mathbf{u} + (\nabla \mathbf{u})^T)] + \mathbf{F} + \rho \mathbf{g} \quad (5)$$

Where ρ [kg/m³] is the fluid density, \mathbf{u} [m/s] is the velocity vector of the fluid, T [K] is the absolute temperature, p [Pa] is the pressure of the fluid, \mathbf{I} [unit less] is the identity matrix, μ [Pa.s] is the dynamic viscosity of the fluid, and \mathbf{F} [N/m³] is the volume force vector.

Any body of any shape when immersed in a fluid flow stream will experience forces from the fluid flow ³⁶⁾. The motion of the particles in fluid flow could be described with Newton's second law ^{35,38)}:

$$\frac{d}{dt}(m_p \mathbf{v}) = \mathbf{F}_t \quad \& \quad \mathbf{v} = \frac{d\mathbf{q}}{dt} \quad (6)$$

where m_p [kg] is the particle mass, \mathbf{v} [m/s] is the velocity of the particle, \mathbf{F}_t [N] is the total force exerted on the particle and \mathbf{q} [m] is the particle position. Here, as presented in equation (7), the total force may include gravitational \mathbf{F}_g , drag \mathbf{F}_D , virtual mass \mathbf{F}_{VM} , pressure gradient \mathbf{F}_P , lift \mathbf{F}_L , and Brownian \mathbf{F}_B forces ³⁵).

$$\mathbf{F}_t = \mathbf{F}_g + \mathbf{F}_D + \mathbf{F}_{VM} + \mathbf{F}_P + \mathbf{F}_L + \mathbf{F}_B \quad (7)$$

The gravitational force is calculated using equation (8). Since the fluid density is also considered, the equation also contains buoyancy force ³⁵).

$$\mathbf{F}_g = m_p g \frac{\rho_p - \rho}{\rho_p} \quad (8)$$

where g [m/s²] is the acceleration of gravity and is ~ 9.8 and ρ_p [kg/m³] is the particle density.

The drag force acts in the direction opposite the relative velocity of the particle with respect to the fluid ³⁵). Drag is essentially a flow loss ³⁶). The drag force is calculated using Stokes drag law equation (9). However, the Stokes drag is applicable for particles travelling through creeping flow, *i.e.* the fluid flow with very low Reynolds number: $0 < Re < 1$ ^{33,35,36,39}). In current study, the fluid in the pores flows at a low velocity, 0.08 [cm/s], with the calculated Reynolds number close to 1.2. Meanwhile, for all particles in this study, the particle relative Reynolds number is less than one in most sections of the filter setup, as seen in Table 3. On the other hand, in the rest of the domains, the relative Reynolds number is not less than one and varies with particle size, as presented in table 3. In such cases, the standard drag correlation that adjusts the drag force based on the relative Reynolds number could be used. The standard drag correlation, *i.e.* the modified Stokes drag force, is calculated according to Stokes drag law and by applying equations (9 to 13) ^{33,35,38}).

$$\mathbf{F}_D = \frac{m_p}{\tau_p} (\mathbf{u} - \mathbf{v}) \quad (9)$$

$$\tau_p = \frac{4\rho_p d_p^2}{3\mu C_D Re_r} \quad (10)$$

$$C_D = \frac{24}{Re_r} \left(1 + \frac{3}{16} Re_r \right) , \quad Re_r \leq 0.01 \quad (11)$$

$$C_D = \frac{24}{Re_r} \left(1 + 0.1315 Re_r^{0.82-0.05w} \right) , \quad 0.01 < Re_r \leq 20 \quad (12)$$

$$C_D = \frac{24}{Re_r} \left(1 + 0.1935 Re_r^{0.6305} \right) , \quad 20 < Re_r \leq 260 \quad (13)$$

where τ_p [s] is the particle velocity response times, C_D is a dimensionless drag coefficient, and $w = \log Re_r$.

The virtual mass and pressure gradient forces would be most significant when the density of the particle is similar or less than the fluid density^{35,40,41}). The virtual mass represents the acceleration of the fluid as it occupies the empty space that a moving particle leaves behind resulting in a virtual increase in particle mass^{35,40}). As shown in Table 2, fluid density is larger than particle density. The virtual increase of the particle mass, i.e. the part of the fluid with higher density, needs to be accelerated up to the particle velocity which on the other hand requires an increase in pressure gradient to accelerate the whole mixture⁴⁰). The virtual mass and pressure gradient terms could be calculated using equations (14), (15) and (16)^{35,41}):

$$\mathbf{F}_{VM} = \frac{1}{2} m_f \frac{d(\mathbf{u} - \mathbf{v})}{dt} \quad (14)$$

$$\mathbf{F}_P = m_f \frac{D\mathbf{u}}{Dt} \quad (15)$$

$$m_f = \frac{1}{6} \pi d_p^3 \rho \quad (16)$$

where m_f [kg] is the mass of the fluid displaced by the particle volume and the material derivative D corresponds to fluid velocity direction.

In a non-uniform velocity field, particles are also subject to lift force^{35,36,39}). The lift force acts along the direction of the gradient of the fluid velocity, i.e. perpendicular to the flow direction^{35,36,39}). In Comsol Multiphysics 6.0, the Saffman (F_{LS}) and the Wall induced (F_{LW}) lift forces are available³⁵). The Saffman lift force is applicable for particles far from the walls. The Wall induced lift force is a specialized formulation that accounts for the effects of the nearby walls as particles travel through the channels³⁵). Therefore, the wall induced drag force was applied to the filter pores, *i.e.* channels, and the Saffman drag force was used for the remaining domains. The Saffman and wall induced drag forces can be calculated as below^{35,39,42}):

$$\mathbf{F}_{LS} = 6.46 r_p^2 L_v \sqrt{\mu \rho \frac{|\mathbf{u} - \mathbf{v}|}{L_v}} \quad (17)$$

$$\mathbf{F}_{LW} = \rho \frac{r_p^4}{D^2} \beta (\beta G_1(s) + \gamma G_2(s)) \mathbf{n} \quad (18)$$

where r_p [m] is the particle radius and L_v [m/s] is the relative velocity, D [m] is the distance between the channel walls, s is the non-dimensionalized distance from the particle to the reference wall divided by D , G_1 and G_2 are functions of non-dimensionalized wall distances and \mathbf{n} is the wall normal at the nearest point on the reference wall.

The Brownian force F_B was ignored for particles larger than one micron as it is believed to be significant only for submicron particles^{38,43}).

3.4 Boundary conditions

The complete list of the boundary conditions for fluid flow and particle tracing studies in the system is given in Table 4. In fluid flow studies: a uniform velocity $1.33 \text{ [cm.s}^{-1}\text{]}$ at the inlet, no slip conditions for the inner walls and symmetry conditions for cut plane walls were considered. In single phase fluid flow in Comsol Mutliphysics 6.0, a no slip wall is a wall where the fluid velocity relative to the wall velocity is zero and the symmetry boundary condition stipulates no penetration and vanishing shear stress³⁴). At the outlet, a zero pressure and no viscous stress were assumed. In fluid flow simulation, in addition to pressure p , the velocity field components u in x , y and z directions were calculated throughout the geometry, according to the transport equations (4) and (5).

In particle tracing studies: particles are released at time zero at the inlet. Here, the initial position of the particles was selected to be random and the initial velocity was set according to the velocity of the fluid at that position. The particles are allowed to stick to the interior walls as soon as they hit the walls. It is believed^{10,11}) that alumina inclusion removal in molten steel consists of two steps: first transport of inclusions by molten fluid to the walls of the filter. Second, sintering of the inclusions to the filter surface and filter walls due to high temperature and high interfacial energy of alumina inclusions in molten steel to each other and to the refractory walls^{10,11,22}).

In particle tracing for fluid flow module, whenever a particle reaches the symmetry wall it leaves the model but from the same position, a same size particle with an incoming velocity that mirrors the outgoing velocity enters the model, i.e. as if the particle had hit a wall with bounce condition³⁵). At the outlet, particles are allowed to freeze once reaching the outlet wall. In particle tracing simulations, particle position q and particle velocity v in x , y and z directions were calculated throughout the geometry, according to the Newtonian formulation in equation (6).

4 Results

4.1 Mesh independence

To obtain the optimum mesh for the CFD modelling, several mesh options were configured and the effects of mesh element sizes on mathematically obtained mass flow rate at a given outlet velocity were compared. A summary of the selected mesh parameters; including the selected mesh type, minimum and maximum element sizes in the domains and boundaries, the total mesh element and calculation time are presented in Table 5. The obtained estimated mass flow rates for each mesh option are illustrated in Figure 3. The CFD estimated mass flow rate obtained with mesh option 7 provided the optimum mesh.

At this point, the average mass flow rate does not improve with further mesh refinement, as shown in Figure 3. Therefore, the solution is considered to be independent of the mesh size. Thus, mesh option 7 was selected for the remaining mathematical modelling work.

4.2 Fluid flow calculations

The mathematically obtained velocity magnitudes and velocity field streamlines through the modelled filter setup are illustrated in Figures 4a and 4b. As shown in the figures, higher velocity magnitudes at the inlet and outlet sections as well as non-uniform velocity streamline in the regions before and after filter pores could be observed. On the other hand, there is a uniform low velocity field in the filter pore channels. To be more specific, fluid enters the inlet with an initial velocity and continues to flow along a relatively straight streamline with a uniform velocity towards the end of the inlet. At this point, fluid freely expands and spreads in the space on the top of the filter, *i.e.* spacer. Here, the streamline and velocity magnitude varies in different parts of the domain. This is due to a sudden change in domain shape from inlet to spacer as well as fluid leaving the spacer to the pores. As shown in Figure 4a, higher velocity magnitudes in the area closer to the inlet could be observed while towards the ends of the spacer in the x-axis, velocity reduces. Furthermore, the fluid initially hits the region of the filter that is in front of the inlet. Then, the rest of the flow is carried out towards the edges while slowing down in momentum. Throughout the pores, the fluid flows at a very slow rate and along a straight streamline towards the end of the pores, as presented in Figure 4b. Thereafter, velocity magnitude gradually increases while the streamlines converge and the fluid flows towards the outlet and leaves the domain.

4.3 Particle tracing in fluid flow

Particle trajectories of the 100, 70, 50, 30, 20, 10, 5 and 1 [μm] alumina inclusions were studied independently of each other. In each study, 100 particles were released at time zero from random initial positions at the inlet due to the fact that their distributions were reported to be non-uniform ¹¹⁾. The particle trajectories were mathematically calculated using equations (6) and (7). Meanwhile, the required preliminary data, e.g. the fluid density, the fluid viscosity and velocity at each grid point were provided by the initially solved fluid flow study step. Enough time was given until there were no active particles in the system, *i.e.* particles were either stuck in the filtration setup or had left the system from the outlet. The required time given to the unsteady particle tracing step was found by trial and error. The predicted particle removal rates, *i.e.* the percentage of the particles removed from simulated molten steel by simulated filtration setup, as a function of particle size is illustrated in Figure 5. Figure 6 illustrates the position of the particles when there is no active particle in the system. It can be observed in the figures that 100 % of the particles larger than 50 [μm] are captured by the filtration setup. Almost all 50 [μm] particles are also captured but from this point as the particle size decreases the particle removal rate also

declines. The non-captured particles travel through the filter pores and channels and continue along the streamline towards the outlet.

5 Discussions

Physical refining of a molten steel melt using a square-celled monolithic extruded alumina filter was simulated. To be specific, the laminar fluid flow of the steel melt was simulated and particle trajectories of the alumina inclusions in the size range of 1 to 100 [μm] were numerically obtained. As illustrated in Figure 4, the fluid flow rates vary and the fluid follows an alternating streamline due to the domain change in the sections of the modelled filter setup. Therefore, particles are exposed to different flow rates in different domains of the filter setup. In total eight case studies were performed and in each study 100 particles were released at time zero from random initial positions at the inlet. As a result, the released particles in the inlet pick up the fluid velocity and initially follow the streamline. However, the particles, due to their size, behave differently along the path in different parts of the setup.

In general, a filtration process could be categorized into surface and depth filtration^{6,11,13,15,16,44–46}. In surface filtration, particles are either removed due to their larger size compared to the filter pores and openings also known as sieving^{6,15,45,46} and/or by clustering of the particles and net formation, i.e. cake filtration, on the top of the filter openings^{6,11,15,16,45,46}. In this region, particles tend to collide and bond. This forms a net of particles that acts as an additional filter which results in removing more particles. On the other hand, particles that are not captured neither by sieving nor by cake filtration, i.e. small size particles, enter the filter pores. Here, depending on the fluid velocity and the type of filter or the path ahead, the particles are either captured in the filter through depth filtration^{6,11,15,16,45,46} or follow the streamline and leave the filter. An effective depth filtration is believed to happen mainly in aggregates or granular beds as well as foam filters, due to the tortuous path the fluid and particles have to flow^{6,45,46}. Here, the tortuous internal pore surface area provide higher probabilities of capturing and retaining particles from a molten metal^{15,44,46}.

It is believed^{10,11,13,15,16} that the particles which enter the pores are mainly captured in the upper section of the filter and close to the filter openings at the entrance. As explained earlier, due to clustering and agglomeration of the inclusions, i.e. net or cake formation, the fluid would be forced to flow only through the free path available. As a result, at the entrance in the top of the filter, the fluid flow streamline would locally experience irregularities and would not be able to follow the streamline in the same manner as CFD predicted in Figure 4. Such streamline irregularities would bring the particles close to the surface of the alumina filter^{6,10,11}. Moreover, it is known that the molten steel does not wet alumina particles. Besides, the dispersed particles in a non-wetting melt tend to reduce the surface tension by transferring themselves to a more stable state with a lower surface energy^{6,10,11}. Consequently, a combination of the above mentioned factors would promote particle impaction to the walls of the filter

when inclusions are in close vicinity of filter surface^{6,10,11,46,47)}. Here, alumina inclusions sinter rapidly to the alumina surface of the filter medium^{6,10,11,46,47)}. As the flow passes this region, the fluid flow would return to its original rather straight streamline. Thus, the remaining small particles would mainly follow the streamline towards the filter exit and the outlet. Therefore, less depth filtration occurs^{10,11,15)} as the particles travel towards the exit of the filter.

In this study, mathematical modeling of particle collisions that result in clustering and agglomerations leading to the net formation, *i.e.* cake formation on the filter, is not yet possible in COMSOL Multiphysics. Thus, such particle-particle interactions were not considered. In addition, fluid-particle interaction is also not included in the model. Therefore, the particle tracing is a one-way coupling study, *i.e.* only the fluid affects the particle motion not vice versa. Regardless of the simulation limitations, the position of the removed particles and the numerically obtained particle removal rate for each particle size are presented in Figures 5 and 6. It can be observed that 100 % of the particles larger than 50 [μm] are captured in the region between the inlet and filter. The particles have about half the density of the molten steel and are rather large to follow the streamline towards the filter openings at such low flow rates. Here, due to the density/buoyancy effect, they float and hit the alumina wall on the top of the filter. Almost all 50 [μm] particles are also captured in the same way as larger particles but from this point as the particle size decreases, less particles are captured due to buoyancy. The non-captured particles enter the filter pores and continue the streamline towards the outlet. It is still a difficult task to create a mathematical model considering particle clustering and agglomeration which results in net or cake formation. Therefore, the depth filtration could not be predicted. In order to make a more reliable prediction, the mathematical model needs to be continuously developed to include more complex physical phenomena.

6 Conclusions

A computational fluid dynamics study; including simulations of both fluid flow and particle tracing of non-metallic alumina inclusions, in the size range of 1 to 100 [μm], from steel melt through a square-celled monolithic alumina filter was conducted. The CFD study was done in two steps. First, the steady state laminar fluid flow, *i.e.* molten steel at 1600°C, was simulated. The solution was calibrated to be independent of the mesh size. Then, particle trajectories were predicted using an unsteady solver based on the results obtained from the first step. Recirculation of the flow in the spacer in the upper section of the filtration setup and/or on the top of the filter leads to removing of large particles from fluid flow. The smaller particles however, follow the streamline along the filter channels and leave the simulated filtration setup from the outlet. The predicted results for particles in the size range ≤ 5 [μm] were compared to the published experimental data. The main conclusions of the study could be summarized as follows:

- The modelled filtration setup could capture 100 % of the particles larger than 50 [μm].
- The percentage of the filtered particles decreases from 98% to 0% in the particle size range of 50 [μm] to 1[μm].
- The current model has a limitation in predicting particle filtration for particles in the size range ≤ 5 [μm].
- Further modeling development of physical filtration is required to include particle clustering and agglomeration which results in net or cake formation.

7 REFERENCES

- 1) A.N. Leonov, M.M. Dechko, *Refractories and Industrial Ceramics*, **40**, 537–542 (1999).
- 2) Christos G. Aneziris, Steffen Dudczig, Marcus Emmel, Harry Berek, Gert Schmidt, Jana Hubalkova, *Adv Eng Mater*, **15**, 46–59 (2013).
- 3) Shahin Akbarnejad, Lage Jonsson, Mark William Kennedy, Ragnhild Elizabeth Aune, Pär Jönsson, *Metallurgical and Materials Transactions B*, **47B**, 2229–2243 (2016).
- 4) Y. Yang, Y. Maeda, M. Takita, H. Nomura, *International Journal of Cast Metals Research*, **10**, 165–170 (1997).
- 5) H. V. Atkinson, G. Shi, *Prog Mater Sci*, **48**, 457–520 (2003).
- 6) J. W. Brockmeyer, L. S. Aubrey, *Ceram. Eng. Sci. Proc.*, **8**, 63–74 (1987).
- 7) Lifeng Zhang, Brian G. Thomas, *ISIJ International*, **43**, 271–291 (2003).
- 8) Lifeng Zhang, Brian G. Thomas, *XXIV National Steelmaking Symposium*, **2**, 138–183 (2003).
- 9) André Luiz, *Integr Med Res*, **7**, 283–299 (2018).
- 10) D. Apelian, R. Mutharasan, S. Ali, *Materials Science and Engineering*, **20**, 3501–3514 (1985).
- 11) S. Ali, R. Mutharasan, D. Apelian, *Metallurgical Transactions B*, **16**, 725–742 (1985).
- 12) R. Dippenaar, *Ironmaking & Steelmaking*, **32**, 35–46 (2005).
- 13) S. Ali, D. Apelian, R. Mutharasant, *Canadian Metallurgical Quarterly*, **24**, 311–318 (1985).
- 14) Ken-ichiro Uemura, Masamitsu Takahashi, Shinji Koyama, Masaki Nitta, *ISIJ International*, **32**, 150–156 (1992).
- 15) Rudolph A. Olson, Luiz C. B. Martins, “Cellular Ceramics: Structure, Manufacturing, Properties and Applications,” 2005, pp.403–415.

- 16) Lucas Nana Wiredu Damoah, Lifeng Zhang, *Metallurgical and Materials Transactions B*, **41**, 886–907 (2010).
- 17) Mark William Kennedy, Shahid Akhtar, Jon Arne Bakken, Ragnhild E. Aune, *Metallurgical and Materials Transactions B*, **44**, 691–705 (2013).
- 18) Sahai Y., *Metallurgical and Materials Transactions B: Process Metallurgy and Materials Processing Science*, **47**, 2095–2106 (2016).
- 19) Niclas Ånmark, Andrey Karasev, Pär Göran Jönsson, *Materials*, **8**, 751–783 (2015).
- 20) T. B. Braun, J. F. Elliott, M. C. Flemings, *Metallurgical Transactions B*, **10**, 171–184 (1979).
- 21) A. McLean, R. G. Ward, Barry Strathdee, *JOM*, **17**, 526–528 (1965).
- 22) S. N. Singh, *Metallurgical and Materials Transactions B*, **5**, 2165–2178 (1974).
- 23) T. Debroy, J. A. Sychterz, *Metallurgical Transactions B*, **16**, 497–504 (1985).
- 24) Lifeng Zhang, W. Pluschkell, *Ironmaking & Steelmaking*, **30**, 106–110 (2003).
- 25) H.B. Yin, H. Shibata, T. Emi, M. Suzuki, *ISIJ International*, **37**, 936–945 (1997).
- 26) Marie-Aline Van Ende, Katholieke Universiteit Leuven, Leuven, 2010.
- 27) L. Bulkowski, U. Galisz, H. Kania, Z. Kudliński, J. Pieprzyca, J. Barański, *Archives of Metallurgy and Materials*, **57**, 363–369 (2012).
- 28) Soumava Chakraborty, Ronald J. O. Malley, Laura Bartlett, Mingzhi Xu, *Proceedings of the 122nd AFS Metalcasting Congress (2018, Fort Worth, TX), American Foundry Society*, (2018).
- 29) Soumava Chakraborty, Missouri University of Science and Technology, Rolla, Missouri, 2020.
- 30) Shahin Akbarnejad, Mohsen Saffari Pour, Lage Tord Ingemar Jonsson, Par Goran Jonsson, *Metallurgical and Materials Transactions B: Process Metallurgy and Materials Processing Science*, **47B**, 197–207 (2017).
- 31) Marc J. Assael, Konstantinos Kakosimos, R. Michael Banish, Jürgen Brillo, Ivan Egry, Robert Brooks, Peter N. Quested, Kenneth C. Mills, Akira Nagashima, Yuzuru Sato, William A. Wakeham, *J Phys Chem Ref Data*, **35**, 285–300 (2006).
- 32) Robert W. Fox, Alan T. McDonald, Philip J. Pritchard, “Introduction to Fluid Mechanics,” Sixth ed., John Wiley & Sons, Inc., 2004.
- 33) Richard W. Johnson, “The handbook of fluid dynamics,” CRC Press & Springer, 1998.
- 34) CFD Module User’s Guide, COMSOL Multiphysics Version 6.0, 2021.
- 35) Particle Tracing Module User’s Guide, COMSOL Multiphysics Version 6.0, 2021.
- 36) White F. M., “Fluid Mechanics,” 7th ed., Mc Graw Hill, 2010.

- 37) A. Haider, O. Levenspiel, *Powder Technol*, **58**, 63–70 (1989).
- 38) Introduction To Particle Tracing Module, COMSOL Multiphysics Version 6.0, 2021.
- 39) P. G. Saffman, *Fluid Mechanics*, **22**, 385–400 (1965).
- 40) Emilio E. Paladino, Clovis R. Maliska, Virtual mass in accelerated bubbly flows.
- 41) Maxey M. R., Riley J. J., *Physics of Fluids*, **26**, 883–889 (1983).
- 42) B. P. Ho, L. G. Leal, *J Fluid Mech*, **65**, 365–400 (1974).
- 43) Amy Li, Goodarz Ahmadi, *Aerosol Science and Technology*, **16**, 209–226 (1992).
- 44) D. Apelian, R. Mutharasan, (1980).
- 45) Klaus Raiber, Peter Hammerschmid, Dieter Janke, *ISIJ International*, **35**, 380–388 (1995).
- 46) L. J. Gauckler, M. M. Waeber, C. Conti, M. Jacob-Duliere, *Jom*, **37**, 47–50 (1985).
- 47) D. Apelian, WH. Sutton, *Superalloys*, 421–432 (1984).

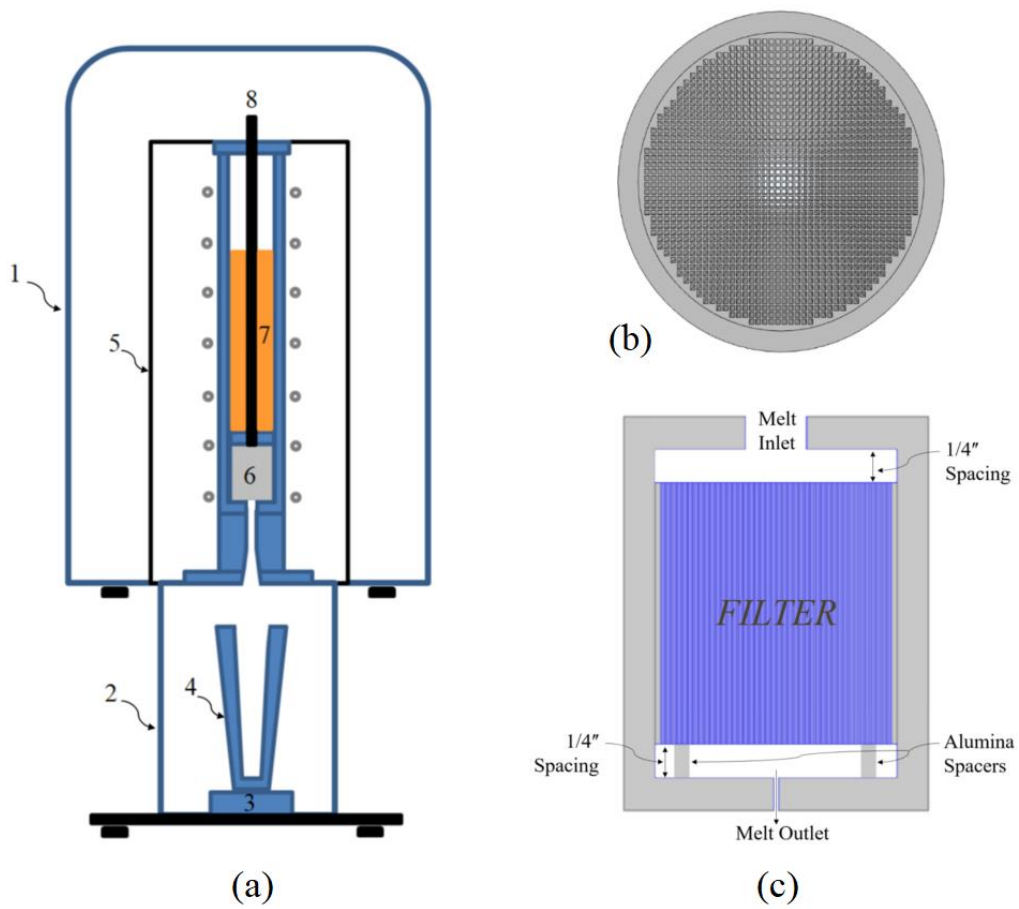


Figure 1: The schematic views of the experimental setup, adapted from references ^{10,11,13}: (a) The experimental apparatus: 1) Furnace Dome 2) Lower Chamber 3) Load Cell 4) Metallic Mold 5) Furnace setup 6) Alumina Filter 7) Steel Melt 8) Alumina Stopper Rod, (b) The cemented monolithic filter used in the experiment , and (c) The Filter setup

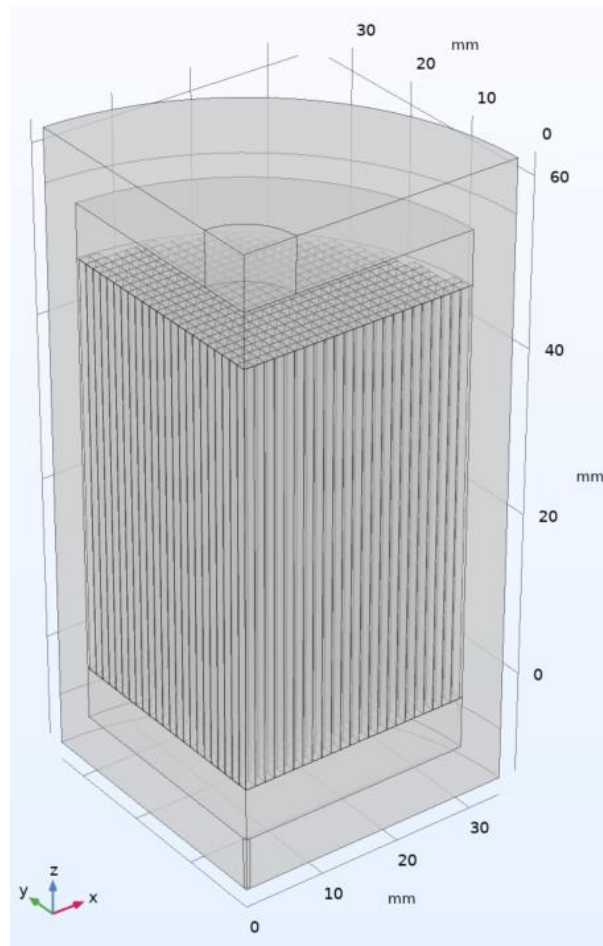


Figure 2: A three-dimensional (3D) view of a quarter of the modelled filter setup

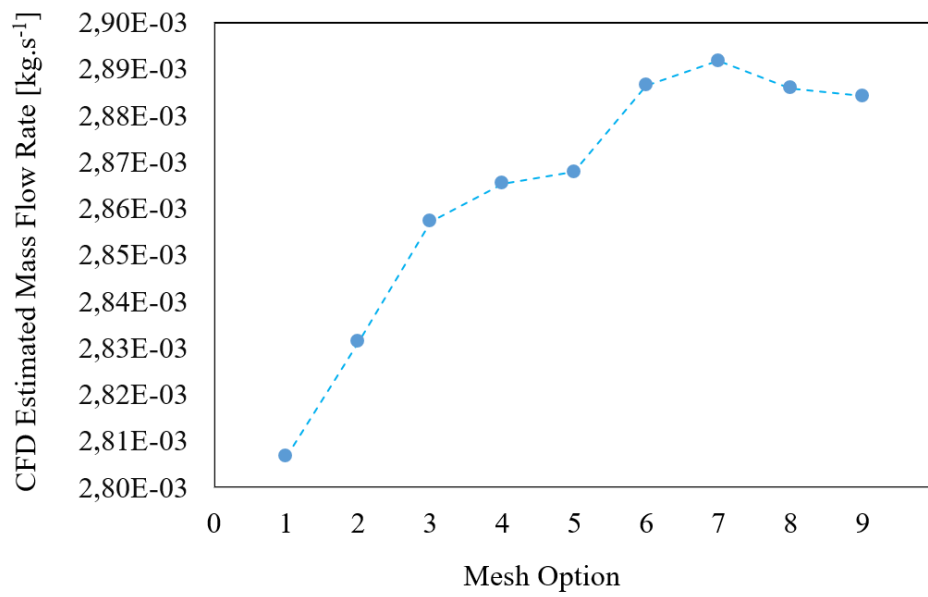


Figure 3: Estimated mass flow rate as a function of mesh option

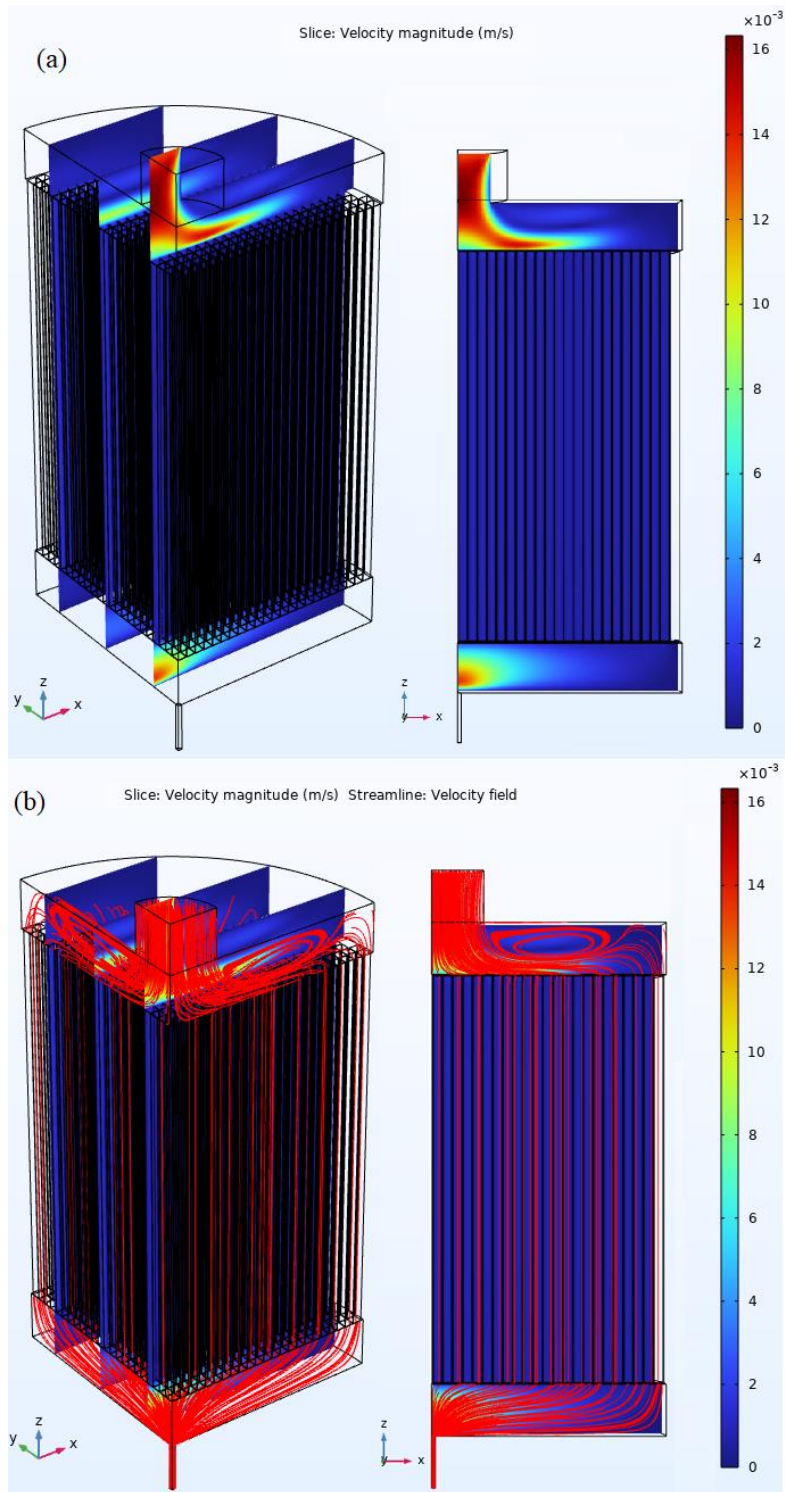


Figure 4: CFD predicted Steel flow properties in the filter setup: (a) Velocity magnitude (b) Velocity streamline

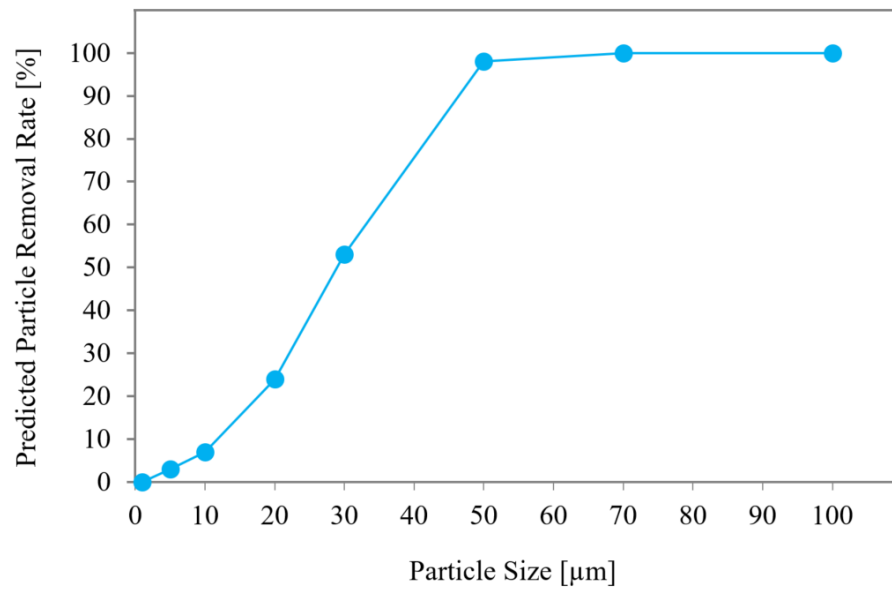


Figure 5: Predicted particle removal rate as a function of particle size

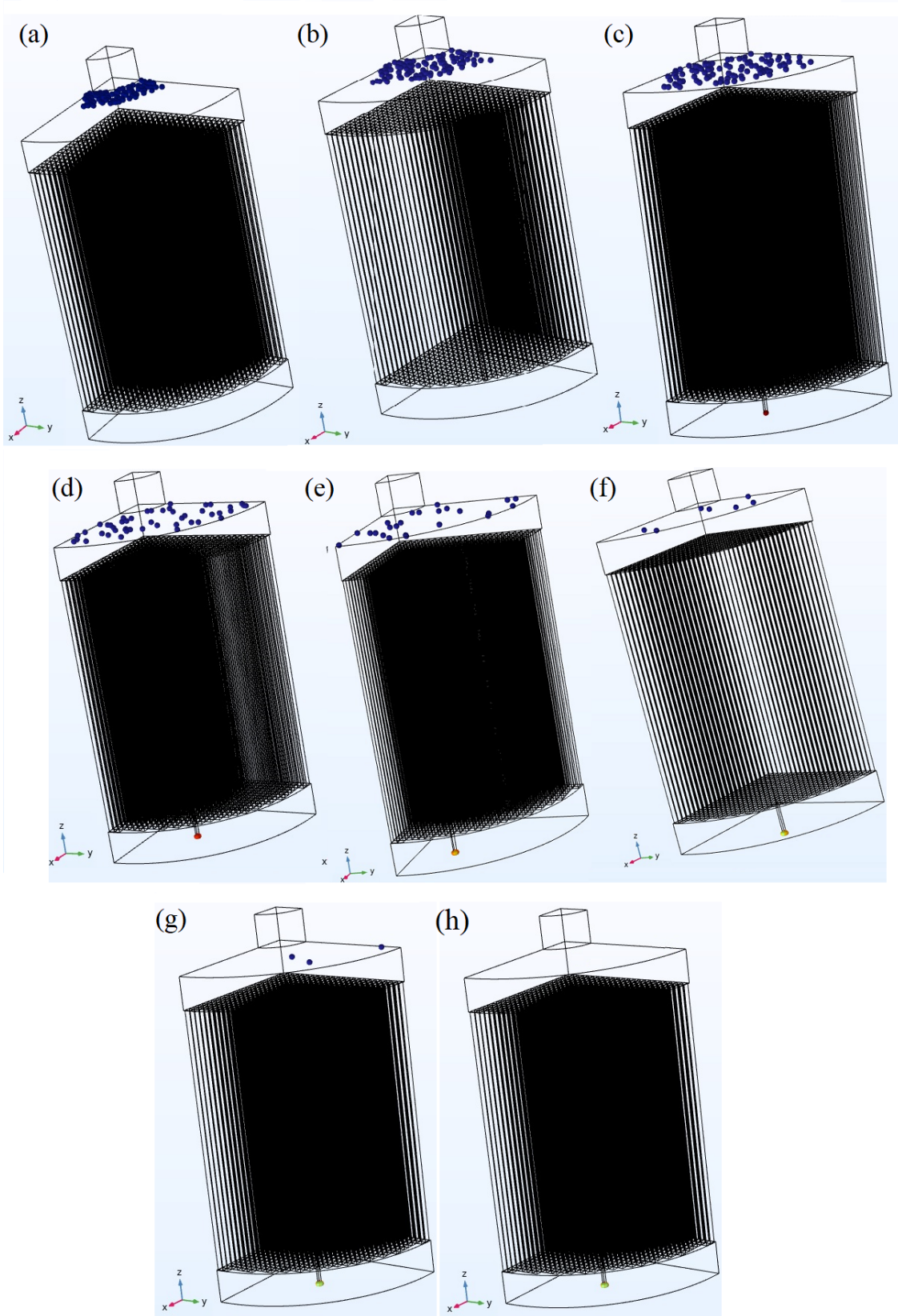


Figure 6: Position of the removed particles: (a) 100 μm , (b) 70 μm , (c) 50 μm , (d) 30 μm , (e) 20 μm , (f) 10 μm , (g) 5 μm and (h) 1 μm

Table 1: Filter setup Dimensions^{10,11,13)}

<i>Section</i>	<i>Diameter [mm]</i>	<i>Height [mm]</i>	<i>Length [mm]</i>	<i>Width [mm]</i>
Inlet	12.7	6.35	N/A	N/A
Spacer between inlet & filter	57.15	6.35	N/A	N/A
Filter	57.15*	50	N/A	N/A
Filter pore	N/A	50	1.15	1.15
Alumina between 2 pores	N/A	50	1.15	0.12
Spacer between filter & outlet	57.15	6.35	N/A	N/A
outlet	1	6.35	N/A	N/A

*: according to the references, there are 400 cells/inch² and the diameter of the filter is 2.25 inches. As a result, the total number of the pores were calculated to be 1590.

N/A: Not Applicable.

Table 2: Steel and Alumina Inclusion properties

<i>Material</i>	<i>Density</i> <i>[kg.m⁻³]</i>	<i>Dynamic</i> <i>viscosity</i> <i>[Pa.s]</i>	<i>Temperature</i> <i>[K]</i>
Steel*	6975	5.2E-03	1873
Alumina	3900	N/A	

*: Properties of the Steel containing 0.012 pct. C, 0.04 Ni was assumed to be the same as Iron at 1873[K] ³¹⁾

Table 3: Calculated Particle Relative Reynolds numbers

<i>Particle Diameter</i> [μm]	<i>Relative Reynolds number</i>		
	Inlet	In a Pore	Outlet
100	1.8	0.1	287
70	1.2	0.8	200
50	0.9	0.05	143
30	0.5	0.03	86
20	0.4	0.02	57
10	0.2	0.01	29
5	0.1	0.005	14
1	0.02	0.001	3

Table 4: Boundary conditions

<i>Section</i>	<i>Inlet</i>	<i>Interior walls</i>	<i>Symmetry walls</i>	<i>outlet</i>
Fluid	$u = -nU_0 \text{ [m.s}^{-1}\text{]}$	$u = 0 \text{ [m.s}^{-1}\text{]}$	$u \cdot n = 0 \text{ [m.s}^{-1}\text{]}$	$P_{\text{ref}} = 0 \text{ [Pa]}$
Particles	$v = v_0 \text{ [m.s}^{-1}\text{]}$ $q = q_0 \text{ [m]}$	$v = 0 \text{ [m.s}^{-1}\text{]}$	$v = v_c - 2(n \cdot v_c)n \text{ [m.s}^{-1}\text{]}$	$v = v_c \text{ [m.s}^{-1}\text{]}$

where n is the boundary normal pointing out of the domain, U_0 is the normal inflow speed ³⁴⁾ v_0 is the particle initial velocity, q_0 is the particle initial position and v_c is the velocity of the incident particle ³⁵⁾.

Table 5: Mesh independence study parameters

<i>Mesh no.</i>	<i>Mesh type</i>		<i>Element size in domains [mm]</i>		<i>Element size in boundaries [mm]</i>		<i>Total Mesh element [millions]</i>	<i>Calculation time [minutes]</i>
	<i>Physics controlled</i>	<i>User controlled</i>	<i>Min.</i>	<i>Max.</i>	<i>Min.</i>	<i>Max.</i>		
1	Coarser	-	6.82	1.7	3.41	1.02	0.26	8
2	Coarse	-	4.43	1.36	2.28	0.682	0.51	5
3	Normal	-	3.41	1.02	1.81	0.341	1.46	12
4	-	√	2.28	0.682	1.81	0.341	1.6	14
5	-	√	1.81	0.341	1.81	0.341	1.71	17
6	-	√	1.26	0.136	1.26	0.136	10.2	308
7	Finer	-	1.81	0.341	0.784	0.0511	47.9	1502
8	-	√	1.54	0.166	0.8	0.08	5.97	107
9	-	√	1.54	0.166	0.784	0.0511	20.68	196